JOURNAL OF PROPULSION AND POWER
Vol. 24, No. 6, November–December 2008

Simulation of Icing on a Cascade of Stator Blades

Sang Lee* and Eric Loth†
University of Illinois at Urbana-Champaign, Urbana, Illinois 61801

DOI: 10.2514/1.37810

Investigations were conducted to examine ice accretion on a cascade of stator blades and its influence on the resulting aerodynamics. In particular, ice shapes and aerodynamic penalties were investigated on a stage 67A stator blade, which represents a part of a turbomachinery compressor stage. A steady Reynolds-averaged Navier–Stokes solver for the airflow was used with a Lagrangian continuous random walk for the droplet trajectory released upstream of the stator blade to predict impingement efficiencies. These results were coupled after finite icing intervals (ca. every 3 min) to update the ice shape around the stator blade using LEWICE. The overall methodology allowed the prediction of the impingement efficiency, the amount of ice accretion, and the adverse effects on the aerodynamic performance. Ice accretion is found to be significantly sensitive to droplet size, integration time, and temperature. However, relatively weak sensitivity was found with respect to the turbulence and angle of attack. Changes in the flowfield due to ice accretion can lead to boundary-layer separation, which causes a reduction in the flow turning angle and mass flow rate as well as an increase in the total pressure loss.

I. Introduction

IN THE past, studies of ice accretion on aircraft aerodynamic surfaces have shown that icing can cause serious performance and safety problems during the course of flight. Reports of aircraft crashes due to ice accretion have led to substantial experimental and computational investigations. Experimental studies on wind turbines have shown a significant loss in power generation [1,2], including thrust reduction in turboprop engines [3], both due to ice accretions on the blades. However, similar research on ice accretion on turbomachinery is not as advanced, even though icing in the engine components can be a concern for engine certification and ice protection system designers [4,5]. There are a number of possible scenarios of the detrimental effects that can result from ice accretion. In an example of a turbofan engine, this could include icing on the fan outlet guiding vanes, which can cause airflow blockage, raising the fan operating line into stall; icing on booster inlet guide vanes, which can reduce the flux of air in the core flow; and ice shedding, which can damage the mechanical components downstream [6,7].

In this study, the effect of ice accretion on the two-dimensional stator cascade in the compressor stage is investigated numerically. In particular, the first stator after the fan is simulated, because this is the part where most ice is accumulated. An outline of the numerical methodology for computing the flowfield and ice-accretion prediction will be discussed, followed by some validation of the numerical tools and the results for various flow conditions.

II. Computational Methodology

Three stages of numerical computation are employed to predict ice accretion and flow changes in the stator cascade (Fig. 1). First, the Reynolds-averaged Navier–Stokes (RANS) solver called WIND [8] is used to compute the steady-state flowfield in the cascade. This code is a structured, multizone, node-centered finite volume method that solves the fully compressible Reynolds-averaged Navier–Stokes equations with a variety of well validated turbulence models. Partial differential equations are modeled in conservative form, wherein the explicit terms are computed using a Roe upwind third-order operator and the implicit terms are computed using a full block operator in the viscous directions and the diagonalized matrix solver in the inviscid directions. The shear stress transport k–ω model is used for turbulence modeling, which is known to predict turbulence reasonably for free-shear flows and boundary layers. GRIDGEN is used to generate the elliptic grids for the cascade. Based on the steady-state WIND flow solution, a program called DROP [9,10] predicts the droplet trajectories in the Lagrangian frame and the impingement efficiency on the surface of the stator based on the continuous random walk model [9] to simulate the effects of turbulent diffusion. This method includes finite turbulent acceleration fluctuations, correction for nonhomogeneous turbulent diffusion, and a local time stepping scheme [9,10]. Next, the impingement efficiency distribution from the droplet trajectory code and the static pressure distributions from the computational fluid dynamics (CFD) code are used in LEWICE [11] to predict the ice accretion on the surface of the stator blade. The ice accretion within a few minutes will change the cross-sectional geometry of the stator blade. Therefore, a new grid is generated for ice-accreted geometry. To allow coupling of the changing geometry and impingement efficiency, a new RANS flow solution is obtained to characterize the aerodynamics of the iced stator blade and the process is repeated until the final integration time is reached. A similar technique using the finite element method by Venkataramani et al. [12] showed that the ice shapes were captured well to a fair degree.

A. Stator Cascade

To simulate the first stage of the stator in a straightforward manner, the upstream condition is idealized as a uniform flow at a fixed angle that represents the effects caused by an upstream rotating fan (Fig. 2). A controlled-diffusion blade called stage 67A [13], which is a replacement of the original double-circular-arc profiles of stator 67, is used for the blade geometry because it is commonly used for compressor blade research [14–17]. The stage 67A blade not only has excellent peak adiabatic efficiency, but it also sustains a wider rage of stall-free incidence than the double-circular-arc blades and keeps the boundary layer thin and free of flow separation up to Mach 0.8 [16]. The cascade represents the midspan of the first stator for a high-bypass turbofan engine, such as the Rolls Royce Trent 884 and the GE90 engines, which have midspan chord lengths of about 4–6 in. [18], thereby yielding chord Reynolds numbers within the range of 400,000–800,000. The flow solution was first computed for validation for the conditions in Table 1 to obtain a flowfield consistent with that of Sanger and Shreeve [16]. Periodic boundary conditions are used to represent an infinite cascade.

The resulting RANS solution is shown in Fig. 3a, in which it can be seen that the boundary layer is thin with no flow separation. Two

Presented as Paper 208 at the AIAA Aerospace Sciences Meeting, Reno, NV, 1 January 2006; received 31 March 2008; accepted for publication 28 June 2008.

*Research Assistant, Aerospace Engineering. Student Member AIAA.
†Professor, Department of Aerospace Engineering. Associate Fellow AIAA.

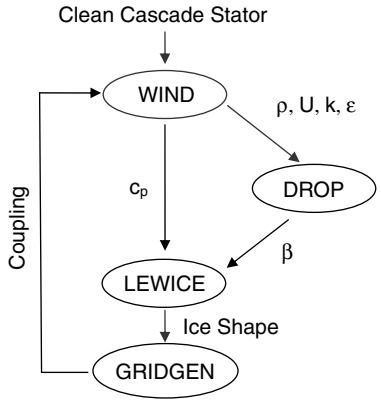

Fig. 1 Schematic of the interval-coupled ice-accretion simulation technique.

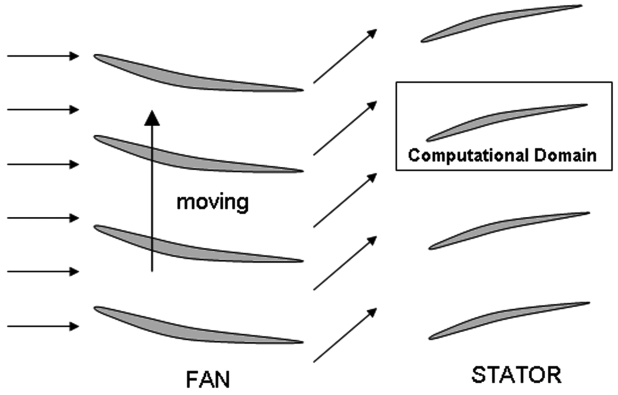

Fig. 2 Stator cascade subject to the upstream fan, for which the computational domain assumes upstream angled flow and uniform droplet distribution. Periodic boundary conditions are imposed on the top and bottom of the domain to represent an infinite cascade.

O-type grids, a baseline grid of 300×100, and a high-resolution grid of 500×120 show nearly identical static pressure coefficient distributions (C_p) in Fig. 3b. The first grid point off the stator surface for the baseline grid is about 2×10^{-5} of the stator chord length. A comparison of the predicted distribution with the experimental data [16] in Fig. 3b shows good agreement, indicating that the flowfield is reasonably accurate and that the 300×100 baseline grid resolution and the turbulence model selection is sufficient. The WIND technique was then employed to compute the flow at typical icing conditions (Table 1).

B. Droplet Impingement Efficiency

The impingement efficiency distribution is obtained for droplets released uniformly upstream of an airfoil using DROP. As the droplet impinges on the airfoil surface over time, the impingement efficiency, β_i, can be obtained as

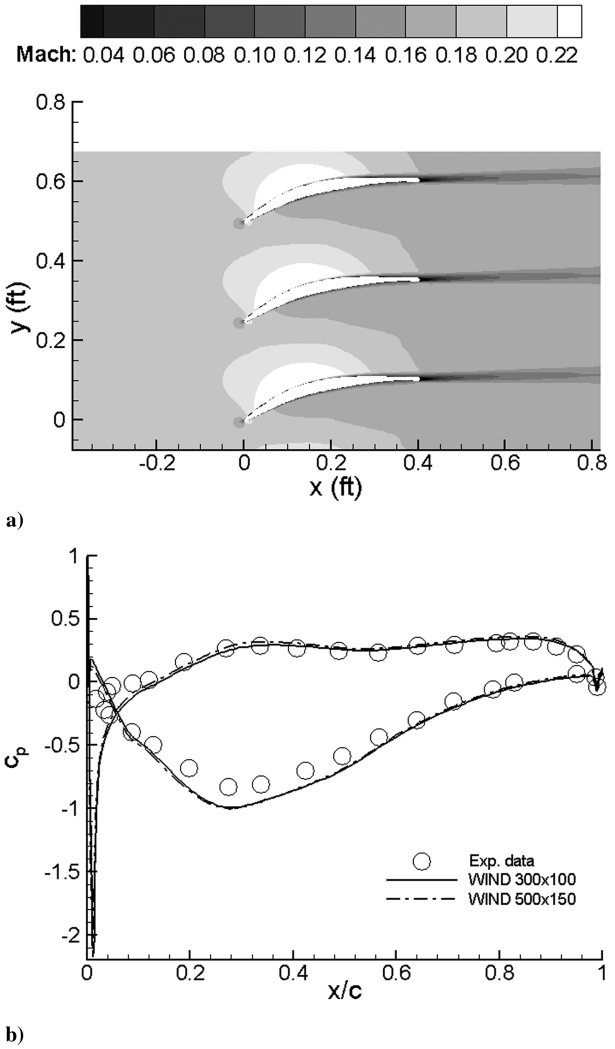

Fig. 3 Flow solution of the stage 67A stator cascade: a) Mach contours, and b) comparison of the static pressure coefficient distribution with the experimental data from [16].

$$\beta_i = (N/S)_i/(N/S)_\infty \tag{1}$$

where $(N/S)_i$ is the number of droplets, N, per unit area passing at the ith surface segment, S, and $(N/S)_\infty$ is the total number of droplets per unit area released upstream. The impingement efficiency, β_i, can be computed for each segment, or bin, over the wrapping distance (s), which is the surface length along of the airfoil's shape. The computational efficiency is improved by using a Gaussian kernel estimator [19], in which each computational droplet is represented as a cloud of physical droplets based on a Gaussian distribution in space with a variance of $3/2$ of the surface segment length scale. This reduces the total number of droplet trajectories that are needed for the convergence of the collection efficiency.

Table 1 Testing condition for the stage 67A stator cascade

Testing conditions	Sanger and Shreeve experiment [16]	Parametric study
Chord length, in.	5.01	
Solidity	1.67	
LE radius, in.	0.0448	
Stagger angle, deg	14.4	
Inlet flow angle, deg	32.95, 40.0, 45.96	
Upstream speed, ft/s	225	200
Altitude, ft	Sea level	10,000
Static temperature, °F	65	−22–30
Reynolds number	583,000	461,000
LWC, g/m^3	Clean	0.54

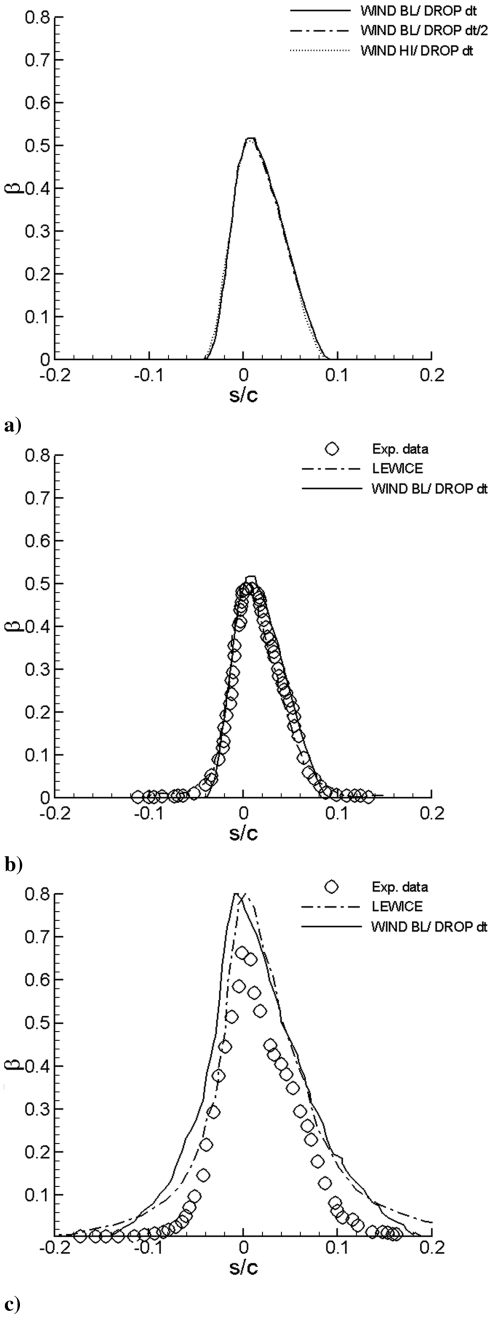

Fig. 4 Impingement efficiency validation for the MS317 airfoil with experimental data [20] comparisons: a) spatial and temporal validation of DROP with a 21 μm median volumetric diameter droplet, where BL represents the 300 × 100 grid, HI represents the 500 × 120 grid, dt is the baseline time step, and dt/2 is the time step reduced by half; b) the 21 μm median volumetric diameter droplet; and c) the 79 μm median volumetric diameter droplet.

A spatial and temporal independence study on impingement efficiency was conducted using: 1) a 300 × 100 baseline grid with a baseline local time step for (Δt) DROP, 2) a 300 × 100 grid with half of the local time step ($\Delta t/2$), and 3) a 500 × 120 high-resolution grid with a baseline local time step (Δt). The results are compared in Fig. 4a, in which only small differences are observed, such that the baseline grid with the local time step is deemed sufficient for our study. As a validation, the numerical impingement efficiency is compared with the experimental data [20] shown in Figs. 4b and 4c for two different droplet sizes. The numerical results from LEWICE and DROP (which used a single droplet size) agree relatively well with the experimental data. However, larger droplets tend to have a splashing effect, which reduces the overall impingement efficiency [20]. Larger droplets experience mass loss due to splashing and breakup during impingement, as shown by the high-speed camera images in Papadakis et al. [20]. However, these effects are not included in LEWICE and DROP, and so Papadakis et al. [20] noted that this would lead to an overprediction of impingement efficiencies by LEWICE. The impingement efficiency predictions from DROP agree closely with LEWICE, which indicates that DROP can be used to predict droplet impingement fluxes for small (nonsplashing) drops.

One way to characterize the influence of droplet size is through the modified inertia parameter (Stokes number), which is defined as

$$St_c = \frac{\tau_p}{\tau_c} = \Psi \frac{d}{c}\left[Re_{p,\infty}^{1/3} - \sqrt{6}\tan^{-1}\left(\frac{Re_{p,\infty}^{1/3}}{\sqrt{6}}\right)\right], \qquad Re_{p,\infty} = \frac{U_\infty d}{\nu_f} \tag{2}$$

where τ_c is the convective time scale based on the chord length, τ_p is the droplet response time scale, Ψ is the ratio of the densities of the droplet to the surrounding air, d is the diameter of the droplet, c is the stator chord length, U_∞ is the freestream velocity, and ν_f is the kinematic viscosity of the fluid [21]. An important aspect of a typical compressor blade such as the stage 67A stator is that the modified inertia parameter (based on chord length) for a given droplet size is typically much larger than that for airfoils as a result of the decreased chord length (Table 2). Therefore, one may expect that the droplet trajectories are less affected by the local streamlines for the stator blades due to higher inertia parameters. In addition, the leading-edge radius of a stator blade is much smaller than that of a typical airfoil (Fig. 5a), which can also cause droplets to collect more at the leading edge in the stator case (as will be shown later).

For a very large droplet, for example, 1000 μm where $St_c \to \infty$, the impingement efficiency should effectively equal the sine of the airfoil surface angle for all regions exposed to droplet impingement. This condition can be used to help validate the DROP trajectories in the high inertia limit. The trajectories are shown in Fig. 6a, in which there is a shadowed area where the droplets cannot reach the top surface so that the predicted impingement efficiency is zero. The impingement efficiency for 1000 μm droplets (without gravity) is shown in Fig. 6b, in which there is very good agreement with the sine of the surface angle of the stator up to $s/c = 1.2$, where s/c is the wrapping distance normalized by the chord.

C. Ice-Accretion Method

Coupling the results from CFD approach with the droplet trajectories, one can simulate ice-shape growth with LEWICE based on impingement efficiency and static pressure distribution. Based on a 3 min interval for ice-shape growth, a new grid is created for the flowfield around the iced geometry. Then a flowfield solution around the ice shape is computed, and the entire process is repeated up to the final time integration of 9 min (Fig. 1).

In a previous paper [22], a comparison was made with an uncoupled approach in which the impingement efficiency and static

Table 2 Inertial parameters for various droplets

Droplet diameter, μm	Modified inertia parameter (Stokes number)	
	MS317 airfoil (36 in. chord)	Stage 67A stator (5 in. chord)
5	0.0037	0.025
20	0.040	0.287
79	0.31	2.33

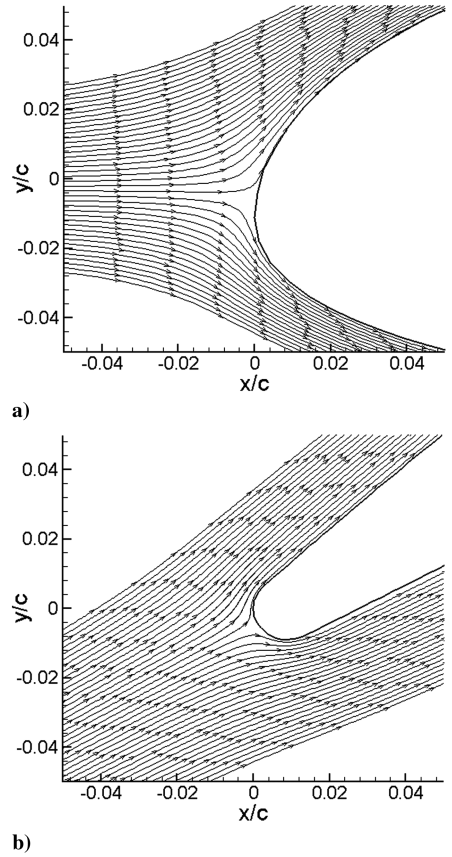

Fig. 5 Comparisons of streamlines for the first 5% of the chord: a) the MS317 airfoil, and b) the stage 67A stator.

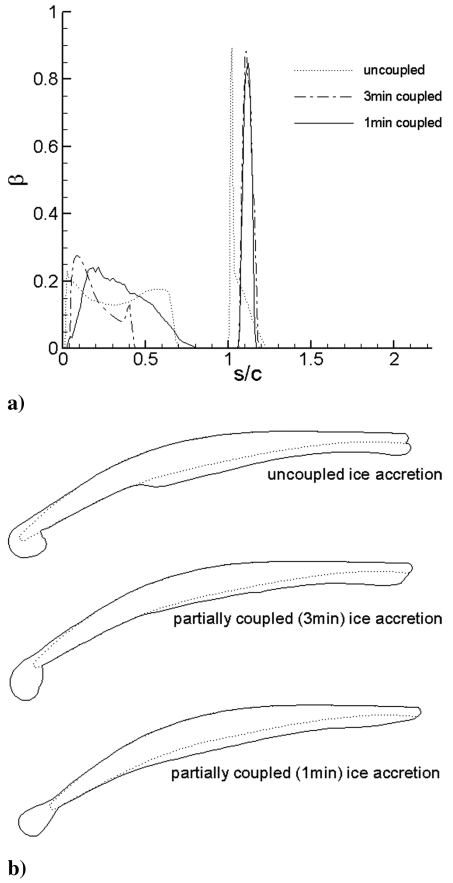

Fig. 7 Coupling effect on the 9 min ice accretion for a 32.95 deg AOA for 20 μm droplets at −4°F: a) impingement efficiency, and b) ice-accretion shapes for the uncoupled and interval-coupled (1 and 3 min) cases.

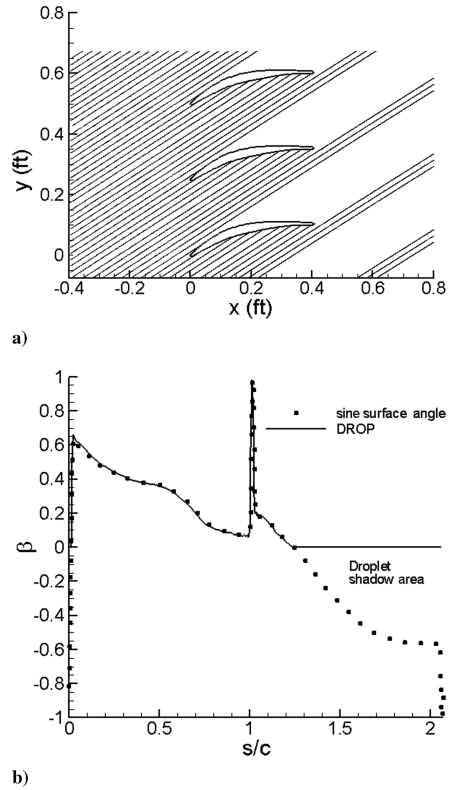

Fig. 6 Validation of the impingement efficiency for a very large droplet size: a) trajectories showing droplet shadow areas with no particles, and b) the sine of the stator surface angle and impingement efficiency.

pressure coefficient from just the clean stator were used to determine the ice shape for the entire 9 min integration. This shows that the basic features of the collection efficiency and the shape are captured by the uncoupled approach but that some differences arise when using the coupled approach, as shown in Fig. 7. In particular, the leading-edge length is much longer for the coupled cases compared with the uncoupled cases. There are also some differences between the shapes for a 3 min baseline coupling and 1 min coupling, for example, the leading edge has a reduced droop angle for the latter. This indicates that 3 min may be a minimum resolution but still yield some temporal resolution dependence. It should be noted that the LEWICE code has not been validated for a coupled approach with even conventional airfoil icing. Thus, more work is needed to understand the impact of coupling. All the results shown for the "parametric study" (Table 1) are for the interval-coupled case using 3 min increments, which allowed reasonable computational efficiency.

III. Results

A. Ice Accretion on Stator

Various conditions were investigated to determine ice accretion and aerodynamic performance sensitivity to turbulence, integration time, droplet size, temperature, and angle of attack. The first study considered the effects on the impingement efficiency and ice-accretion shape of droplet trajectories with and without turbulent diffusion included. This is shown in Fig. 8 for a 5 μm droplet, for which the turbulent diffusion is expected to be strongest. The baseline flow conditions include a 40.0 deg angle of attack (the design angle for the stage 67A stator) at −4°F (a temperature at which icing effects are particularly important). Compared with the nonturbulent trajectory case, the turbulent impingement efficiency

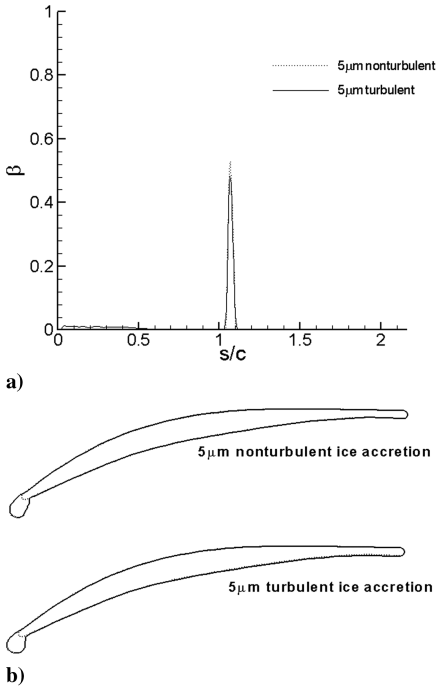

Fig. 8 Impingement efficiency for the turbulent and nonturbulent trajectories for 5 μm droplets at −4°F and a 40.0 deg AOA after 9 min and the parametric study conditions of Table 1: a) impingement efficiency, and b) final iced geometry.

produces a reduced leading-edge peak and gives a nonzero impingement on the pressure side of the stator (s/c from 0–0.5), as shown in Fig. 8a. These effects are due to the turbulent boundary layer, where some of the droplets trajectories are driven by turbulent diffusion into the surface of the stator (whereas the nonturbulent case had a β of zero for an s/c of 0–0.5). As a result, the turbulent case has somewhat smaller ice accretion at the leading edge (Fig. 8b), though the resulting ice-shape geometries are quite similar overall. As such, adding turbulence to the trajectories of the droplet gave only a weak impact (even weaker for large droplet sizes), but was used for all remaining cases for consistency.

The next study examined the final time integrations of 3, 6, and 9 min for 79 μm droplets released for a 40.0 deg angle of attack at a −4°F ambient temperature. The results are shown in Fig. 9, in which it can be seen that the evolution is significant and nonlinear in some places. The latter aspect is due to the coupling between the flowfield and the ice accretion, where a shadow region forms behind the leading edge after 3 min.

The variation due to droplet size is shown more clearly in Fig. 10, in which larger droplet sizes produce larger ice accretions. Higher peaks of the impingement efficiency at the leading edge occur for large droplet sizes (due to higher Stokes numbers). This is because smaller droplets have less inertia and, thus, are more likely to follow the flow and not impinge on the blade. The larger inertia cases cause the ice to grow larger and with a more downward direction. This downward growth is further enhanced by incoming droplets shadowing the region aft the leading edge.

Temperature can also be important to ice-accretion size and shapes, as shown in Fig. 11. For a fixed liquid water content of air (LWC), ice formation is greatly reduced for static temperatures near freezing (28°F) compared with a 12°F case, because the colder case has less melting. This is consistent with airfoil icing whereby ice growth increases with lower temperatures for a fixed LWC. However, further decreases in static temperature (ranging from 12 to −22°F) yield very similar ice shapes, because the freezing fraction is near unity for these temperatures (and equal to unity for temperatures of 6.5°F or less). Although the LWC in the study was held constant, it should be noted that colder temperatures tend to yield lower LWC values and, thus, reduced ice accretion.

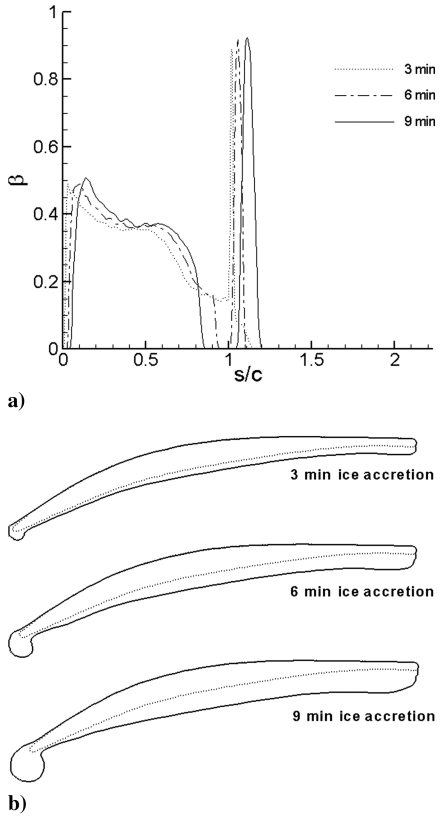

Fig. 9 Ice-accretion growth with respect to time for a 79 μm droplet at −4°F and a 40.0 deg AOA: a) impingement efficiency, and b) ice-accretion shapes at 3 min intervals.

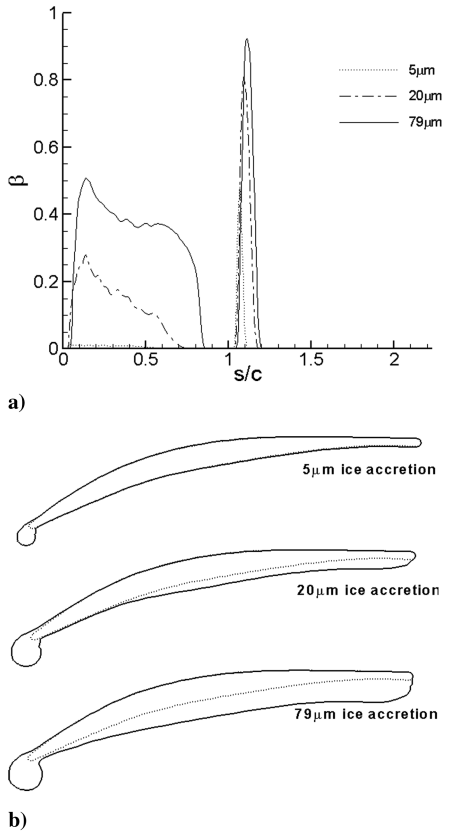

Fig. 10 Droplet size effect on ice formation for −4°F and a 40.0 deg AOA after 9 min: a) impingement efficiency, and b) ice accretion for different droplet sizes.

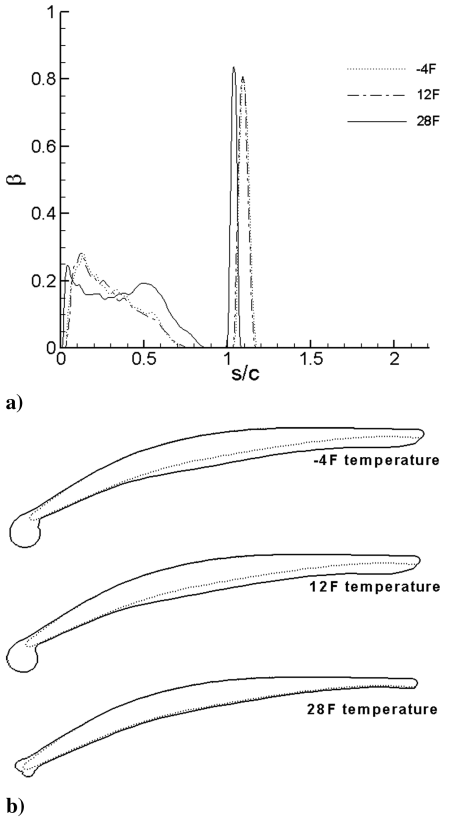

Fig. 11 Comparison of ice formed after 9 min at different temperatures for 20 μm droplets at a 40.0 deg AOA: a) impingement efficiency, and b) ice accretion for different temperatures.

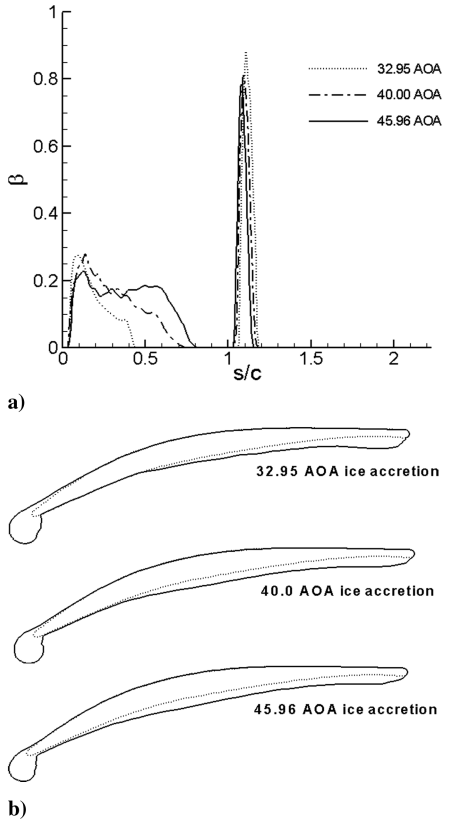

Fig. 12 Angle of attack effect on the 9 min ice accretion for 32.95, 40.0, and 45.96 deg for 20 μm droplets at −4°F: a) impingement efficiency, and b) ice accretion for different angles.

Lastly, the angle of attack effect on the stator ice accretion was investigated for three different angles of attack (AOA); 32.95, 40.0, and 45.96 deg. The smallest angle causes the bottom surface to be almost parallel with the upstream flow, where some ice is accumulated on the top surface near the leading edge as shown in Fig. 12b. This 32.95 deg case yields the largest ice accretion at the leading edge but also more rearward ice accretion on the pressure side surface aft the leading edge (due to camber). As the angle increases, there is a thickening of the ice layer on the bottom surface near the midchord whereas near the trailing edge it becomes thinner. However, the differences are quite modest given the 13 deg angle change between the three cases.

B. Cascade Aeroperformance with Icing

Based on the iced airfoil shapes examined, aerodynamic changes due to ice accretions are investigated. Flow visualization of the leading-edge and trailing-edge flowfields are shown in Figs. 13 and 14 for clean and iced stators. In particular, Mach contours are plotted for the 32.95 deg angle of attack for a clean stator (Fig. 13a) and the 79-μm-droplet ice-accreted stator (Fig. 14a). Large ice accretion at the leading edge causes major flow separation, whereas the clean stator shows almost no flow separation. Flow separation is detrimental as it can lead to stagnation pressure losses and mass flow rate losses through the cascade. Shown in Figs. 13b and 14b, the overall direction of the trailing-edge streamlines for the clean stator is almost at 0 deg, whereas the streamline direction is upward for the iced stator case, indicating suboptimal flow turning.

To quantify these effects, three performance parameters are defined. An average flow turning angle ($\bar{\alpha}$) is computed based on the integration of the local flow angles over the cascade exit, where v_{exit} and u_{exit} are the normal and streamwise velocities, respectively, and n is the number of grid points in the normal direction. The dimensionless total pressure loss ($\bar{\omega}$) is computed by mass averaging the stagnation pressure loss between the inflow and the cascade exit and normalizing this by the upstream dynamic head, where P_{Tin} and

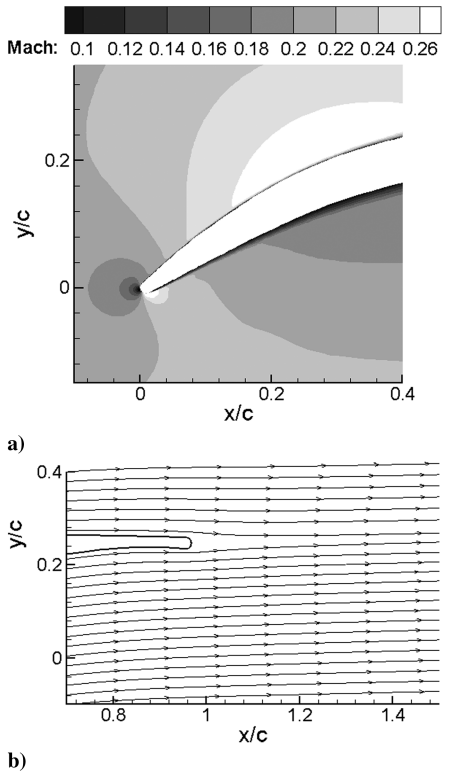

Fig. 13 Mach contours and streamlines for the clean stator for −4°F and a 32.95 deg AOA: a) Mach contours of the clean stator, and b) streamlines for the clean stator.

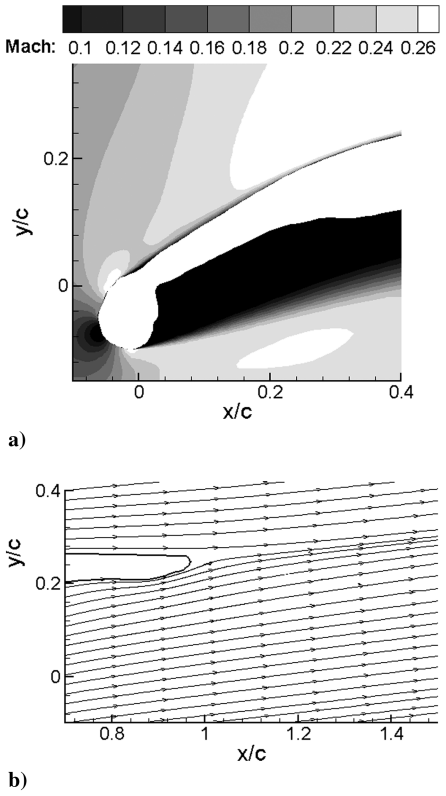

Fig. 14 Mach contours and streamlines for the 79 μm droplet iced stator for −4°F and a 32.95 deg AOA after 9 min: a) Mach contours of the iced stator, and b) streamlines for the iced stator.

P_{Texit} are the stagnation pressure at the inflow and exit, respectively, and P_{in} is the pressure at the inflow. Finally, a mass flow ratio ($\bar{m}$) is computed as the ratio of the mass flow rate through the iced stator cascade, $\dot{m}_{\text{iced}}$, normalized by the mass flow rate of the clean case, $\dot{m}_{\text{clean}}$, for a fixed exit and entrance pressure.

$$\bar{\alpha} = \frac{1}{n}\sum \tan^{-1}(v_{\text{exit}}/u_{\text{exit}}) \tag{3}$$

$$\bar{\omega} = \frac{\bar{P_{\text{Tin}}} - \bar{P_{\text{Texit}}}}{\bar{P_{\text{Tin}}} - P_{\text{in}}} \tag{4}$$

$$\bar{m} = \frac{\dot{m}_{\text{iced}}}{\dot{m}_{\text{clean}}} \tag{5}$$

In general, it is desirable to have low values for the turning angles and high values for the remaining parameters, as this would indicate that the stators have achieved high performance in turning the flow with little loss in stagnation and little blockage.

Table 3 Aeroperformance for various conditions

Case			k/c	$\bar{\alpha}$	$\bar{\omega}$	$\bar{m}$
AOA, deg	Diameter, μm	Temp., °F				
32.95	Clean	−4	0.000	1.3	0.06	1.00
32.95	50	−4	0.059	3.7	0.15	0.94
32.95	20	−4	0.089	6.7	0.23	0.89
32.95	79	−4	0.094	8.2	0.31	0.82
32.95	20	30	0.009	2.5	0.10	0.93
40.00	Clean	−4	0.000	1.3	0.05	1.00
40.00	5	−4	0.033	3.8	0.13	0.94
40.00	20	−4	0.081	6.8	0.16	0.90
40.00	79	−4	0.090	8.4	0.19	0.89
40.00	20	28	0.024	3.0	0.12	0.96

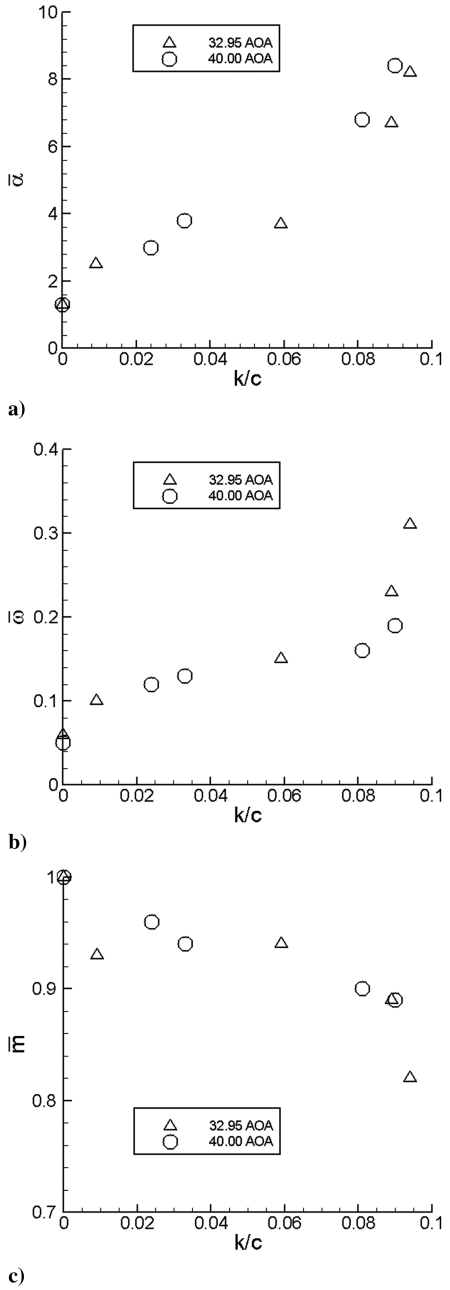

Fig. 15 Performance parameter dependence on ice-shape size: a) average turning angle degrees vs nondimensional horn length, b) total pressure loss coefficient vs nondimensional horn length, and c) average mass ratio vs nondimensional horn length.

The resulting performance parameters are shown in Table 3. The clean cases for both the 32.95 and 40.0 deg angles of attack yield an efficient stator flow, which gives an average flow turning angle close to zero and a low total pressure loss performance. For the iced stator cases, the flow turning angle and the nondimensional total pressure loss were found to increase as the amount of ice accretion increased. This result was attributed primarily to the leading-edge flow separation, which led to turning angles as high as 8 deg and pressure loss parameters as high as 31%. Decreases in the mass flow ratio were found to occur as accretion became more severe with values as low as 82% of the clean airflow rate, where similar results were obtained for inlet icing [23]. It is interesting that the higher-loaded 40.0 deg angle of attack had better icing performance in terms of total pressure loss and mass flow rate than the 32.95 deg case. Good correlation is found between the nondimensional horn length (k/c) and the average flow turning angle ($\bar{\alpha}$), and the total pressure loss coefficient ($\bar{\omega}$) and the mass flow ratio ($\bar{m}$), as shown in Fig. 15. These results indicate that

increasing k/c is generally detrimental with respect to all three performance parameters, particularly once k/c is greater than 8%.

IV. Conclusions

Simulations of icing on cascade stator blades have been conducted to study the effect of ice accretion on aerodynamic performance. In this study, an interval-coupled method of predicting ice accretion has been used, which integrates the ice growth with the static pressure distribution and impingement efficiency distribution. Because of the decreased chord length, the stator blades have higher Stokes numbers (modified inertia parameter) than typical aircraft airfoils for a given droplet size. High peaks of impingement efficiency at the leading edge are due to these larger Stokes numbers, which do not allow the droplet to navigate around the leading edge. Such high peaks produce large ice accretion at the nose of the stator, which results in major flow separation, especially for large droplet sizes and low temperatures. Such flow separation increases the total pressure loss and flow turning angle, which can be detrimental to the performance of the rotors and stators downstream. Furthermore, the reduced mass flow rate caused by ice accretion indicates significant flow blockage effects. These detrimental effects can be extreme once the horn height (maximum ice thickness) exceeds 8% of the chord length. However, additional validation and temporal convergence studies are needed for this interval-coupled approach. In particular, experiments of ice accretion on cascades are needed.

Acknowledgments

We would like to acknowledge M. Bragg and A. Broeren, the support of the Ohio Space Institute, and the technical input from General Electric, BF Goodrich, and the NASA Glenn Research Center. The computations were performed with the support of the National Center for Supercomputing Applications and UIUC Copper Linux Cluster Systems.

References

[1] Hochart, C., Fortin, G., Perron, J., and Ilinca, A., "Icing Simulation of Wind-Turbine Blades," AIAA Paper 2007-1373, 2007.

[2] Gillenwater, D., Masson, C., and Perron, J., "Wind Turbine Performance During Icing Events," AIAA Paper 2008-1344, 2008.

[3] Dumont, C., Pellicano, P., Smith, T., and Riley, J., "Results from a Full-Scale Propeller Icing Test," AIAA Paper 2008-0432, 2008.

[4] Venkataramani, K., McVey, L., Holm, R., and Montgomery, K., "Inclement Weather Considerations for Aircraft Engines," AIAA Paper 2007-0695, 2007.

[5] Venkataramani, K., Plybon, R., Holm, R., and Krupp, B., "Aircraft Engine Icing Model," AIAA Paper 2008-0440, 2008.

[6] Mason, J., Strapp, W., and Chow, P., "Ice Particle Threat to Engines in Flight," AIAA Paper 2006-0206, 2006.

[7] Rasmussen, R., Wade, C., Hage, F., Ladolt, S., Tryhane, M., Cole, J., Ramsay, A., Fleming, D., Moore, R., Davis, A., Reis, B., Lisi, T., Kjolleberg, M., and Rosenlund, K., "Ingesting by Jet Engines," *AIAA Journal*, Vol. 43, No. 5, 2006, pp. 1448–1457.

[8] Nelson, C. C., and Power, G. D., "CHSSI Project CFD-7: The NPARC ALLIANCE Flow Simulation System," AIAA Paper 2001-0594, 2001.

[9] Bocksell, T., and Loth, E., "Discontinuous and Continuous Random Walk Models for Particle Diffusion in Free-Shear Flows," *AIAA Journal*, Vol. 39, No. 6, 2001, pp. 1086–1096. doi:10.2514/2.1421

[10] Bhargava, C., Loth, E., and Potapczuk, M., "Numerical Simulation of Icing Clouds in the NASA Glenn Icing Research Tunnel," AIAA Paper 2004-0563, 2004.

[11] Wright, B., "Validation Results for LEWICE 3.0," AIAA Paper 2005-1243, 2005.

[12] Venkataramani, K., Mallina, R., Shamara, P., and Oliver, M., "Dynamics of Icing in Aircraft Engines," AIAA Paper 2007-0905, 2007.

[13] Sanger, N. L., "The Use of Optimization Techniques to Design Controlled-Diffusion Compressor Blading," *Journal of Engineering for Power*, Vol. 105, April 1983, pp. 256–264.

[14] Hobbs, D. E., and Weingold, H. D., "Development of Controlled Diffusion Airfoils for Multistage Compressor Application," *Journal of Engineering for Gas Turbines and Power*, Vol. 106, April 1984, pp. 271–278.

[15] Dunker, R., Rechter, H., Starken, H., and Weyer, H., "Redesign and Performance Analysis of a Transonic Axial Compressor Stator and Equivalent Plane Cascades with Subsonic Controlled Diffusion Blades," *Journal of Engineering for Gas Turbines and Power*, Vol. 106, April 1984, pp. 279–287.

[16] Sanger, N. L., and Shreeve, R. P., "Comparison of Calculated and Experimental Cascade Performance for Controlled-Diffusion Compressor Stator Blading," *Journal of Turbomachinery*, Vol. 108, July 1986, pp. 42–50.

[17] Shreeve, R. P., Elazar, Y., Dreon, J. W., and Baydar, A., "Wake Measurements and Loss Evaluation in a Controlled Diffusion Compressor Cascade," *Journal of Turbomachinery*, Vol. 113, No. 4, Oct. 1991, pp. 591–599. doi:10.1115/1.2929120

[18] Cumpsty, N., *Jet Propulsion—Simple Guide to the Aerodynamic and Thermodynamic Design and Performance of Jet Engines*, Cambridge Univ. Press, New York/London/ Cambridge, England, U.K., 1997, pp. 47–49.

[19] Silverman, B. W., *Density Estimation for Statistics and Data Analysis*, Chapman & Hall, London, 1986, Chaps. 2–3

[20] Papadakis, M., Rachman, A., and Wong, S., "An Experimental Investigation of SLD Impingement on Airfoils and Simulated Ice Shapes," Society of Automotive Engineers Paper 2003-01-2129, June 2003.

[21] Putnam, A., "Integrable Form of Droplet Drag Coefficient," *American Rocket Society Journal*, Vol. 31, Oct. 1961, pp. 1467–1468.

[22] Lee, S., Loth, E., Broeren, A., and Bragg, M., "Simulation of Icing on a Cascade of Stator Blades," AIAA Paper 2006-208, 2006.

[23] Jin, W., and Taghavi, R., "Computational Study of the Effects of Ice Accretions on the Flowfields in the M2129 S-Duct Inlets," AIAA Paper 2008-0075, 2008.

V. Yang
Editor-in-Chief